https://doi.org/10.26599/FRICT.2026.9441338

Research Article

Synergy of ternary lubricants and biomimetic honeycomb textures: Stagewise intelligent lubrication and protection from 25 to 800 °C

Yuhang Zhang [a, b], Yaoning Sun [a, *], Zhenyu Bu[b], Xiujuan Fan [b], Canwei Han [b], Yizhe Lv [b], Chunfeng Ma [c], Jiansen Pan [c], Chunming Deng [b], Shuangjian Li [b, *]

a. School of Mechanical Engineering, Xinjiang University, Urumqi, 830017, China

b. Institute of New Materials, Guangdong Academy of Sciences, National Engineering Laboratory for Modern Materials Surface Engineering Technology, Guangdong Provincial Key Laboratory of Modern Surface Engineering Technology, Guangzhou, 510651, China

c. Faculty of Materials Science and Engineering South China University of Technology, Guangzhou, 510640, China

Received: August 18, 2026; Revised: November 9, 2026; Accepted: November 18, 2026

© The Author(s) 2026.

Just Accepted

*Corresponding author.
E-mail address: synzxd2000@xju.edu.cn (Y. S); lishuangjian114@163.com (S. L)

Abstract: Wide-temperature adaptive coatings are critical for mitigating tribological failure in marine and aerospace systems. Conventional Cr_3C_2-NiCr coatings offer excellent wear resistance and oxidation stability, but their intrinsically poor self-lubrication limits practical engineering applications. Herein, we developed a hybrid "laser-textured reservoir + vacuum infiltration" strategy to engineer biomimetic honeycomb microstructures on Cr_3C_2-NiCr coatings as in situ reservoirs for B_2O_3/Bi_2O_3/C ternary solid lubricant. The coating achieved average friction coefficients of 0.08, 0.14, and 0.12 at 25 °C, 400 °C, and 800 °C, corresponding to 90.5%, 75.4%, and 76.9% reductions relative to the unmodified counterpart, and maintained stable performance after four consecutive wide-temperature thermal cycles. Remarkably, after four thermal cycles at 800 °C, the wear rate of the novel composite coating (0.15×10^{-5} $mm^3/(N \cdot m)$) is two orders of magnitude lower than that of the pristine coating (13.86×10^{-5} $mm^3/(N \cdot m)$). A stagewise intelligent synergistic lubrication mechanism was elucidated: room-temperature graphite sliding, medium-temperature multiphase synergy, and high-temperature dual-glaze-layer protection. The high-temperature stage exhibits fourfold protective functions: fourfold protective functions: liquid lubrication provided by molten B_2O_3/Bi_2O_3; wear-debris encapsulation by the liquid film enveloping wear debris; oxidation barrier by the glaze layer blocking oxygen diffusion into the coating and graphite interior; and structural support provided by the inner nanocrystalline oxide framework. Molecular dynamics simulations revealed the atomic-scale crystalline-to-amorphous transformation of B_2O_3/Bi_2O_3 at elevated temperatures. This work provides a robust fabrication strategy and novel insights into the design of next-generation high-performance, wide-temperature-range intelligent adaptive lubricating coatings.

Keywords: Cermet coating; Biomimetic laser texturing; Ternary solid lubricant; High-temperature tribology; Wide-temperature self-lubrication; Synergistic protective mechanism

1. Introduction

As power systems in marine engineering and aerospace advance toward higher operating parameters and longer service lives, their critical moving components are frequently subjected to severe temperature fluctuations spanning from room

Just Accepted

temperature to over 800 °C [1-5]. Wear failures induced by high-temperature oxidation and lubrication breakdown have emerged as a critical bottleneck limiting operational reliability [6-8]. Cermet coatings, exemplified by Cr_3C_2-NiCr fabricated via high-velocity oxy-fuel (HVOF) spraying, integrate exceptional hardness with outstanding oxidation resistance, positioning them as ideal candidate materials for wear-resistant applications across a broad temperature range [9-13]. Nevertheless, their inherently insufficient self-lubricating capability leads to elevated coefficients of friction (COF) and catastrophic wear during wide-temperature-range service, severely hindering their further deployment under extreme operating conditions.

To address this challenge and endow Cr_3C_2-NiCr coatings with superior self-lubricating properties, researchers have attempted to incorporate composite lubricants into the feedstock powders [14-17]. Su et al. fabricated Ag/BaF_2·CaF_2-Cr_3C_2-NiCr composite coatings that exhibited significantly reduced COFs over 25–800 °C. However, such composite strategies typically come at the expense of the coatings' mechanical integrity and high-temperature stability [18]. Additionally, the rapid migration of Ag at elevated temperatures compromises the long-term lubrication effectiveness at medium and low temperatures [19-22]. Consequently, achieving sustained lubrication over a wide temperature range while preserving the mechanical integrity of the coatings remains the core challenge for this material system. Laser texturing technology offers a promising approach to balance lubrication longevity and load-bearing capacity [23-26]. By engineering controllable micro/nanostructures on material surfaces as lubricant reservoirs, a continuous lubricant supply and wear debris entrapment can be achieved, thereby tailoring the tribological properties of materials while maximally preserving the intrinsic mechanical performance of the pristine coatings [27-29]. Kong et al. and Wang et al. independently verified the efficacy of textured structures in capturing wear debris and storing composite lubricants [30,31]. Nonetheless, relying solely on microstructural reservoirs, without a matching high-performance, wide-temperature-range lubricant system, remains insufficient to achieve effective lubrication throughout the entire temperature cycle from room temperature to elevated temperatures.

In response to the demand for wide-temperature-range lubrication, designing multicomponent composite lubricants constitutes another effective strategy [32,33]. An ideal composite system should possess low shear strength at low temperatures and form

Just Accepted

glaze layers with simultaneous lubricating and antioxidative functions at high temperatures. The unique temperature-dependent fluidization and high-temperature oxidation resistance of certain low-melting-point oxides have attracted considerable attention [34-37]. Among them, B_2O_3 (melting point ~450 °C) can form a glassy fluid lubricating film at elevated temperatures [38]. Bi_2O_3 also has a relatively low melting point (~825 °C) and can form a eutectic phase with B_2O_3 at an even lower temperature, while exhibiting excellent high-temperature anti-adhesion and oxidation resistance [39]. Sun et al. found that the B_2O_3 glass phase generated during high-temperature friction of WB-Co coatings was one of the primary contributors to reduced COF, and the liquid glass phase demonstrated exceptional high-temperature oxidation resistance [40]. Shao et al. confirmed that the addition of Bi_2O_3 promoted the formation of lubricating glaze layers and delayed the high-temperature oxidation of MoS_2 [41]. However, their work only involved the binary MoS_2/Bi_2O_3 system, which has notable limitations in oxidation resistance and effective temperature range. Multicomponent composites may further extend the applicable temperature range of this antioxidative protection mechanism. The combination of B_2O_3 and Bi_2O_3 can further lower the melting point (eutectic point ~620 °C), promote glass phase formation, and provide fluid lubrication and antioxidative properties at lower temperature gradients [42]. Graphite, on the other hand, delivers excellent solid lubrication in the medium and low temperature ranges but suffers from poor high-temperature oxidation resistance [43-46]. Inspired by this, the $B_2O_3/Bi_2O_3/C$ ternary composite holds great promise for constructing a synergistic system with complementary advantages: the dense glass phase formed by B_2O_3/Bi_2O_3 at high temperatures can not only provide liquid-phase lubrication but also "encapsulate" and protect graphite from high-temperature oxidation, while graphite compensates for the lubrication demand in the low-temperature regime. This ternary strategy provides a new avenue for overcoming the temperature range limitations of single lubricating phases.

Inspired by the hexagonal honeycomb structure in nature, which exhibits exceptional storage efficiency and structural stability, this design has shown great potential for enhancing the tribological properties of coatings [47,48]. However, the synergistic mechanism between biomimetic honeycomb textures and the $B_2O_3/Bi_2O_3/C$ ternary lubricant over a wide temperature range remains poorly understood. Different from our previous work [28], which focused on process feasibility at room temperature

Just Accepted

and 800 °C using a B_2O_3/Bi_2O_3 filler, this study innovatively combines biomimetic honeycomb textures with the B_2O_3/Bi_2O_3/C ternary composite lubricant, providing a simple yet effective strategy for tailoring the tribological properties of Cr_3C_2-NiCr coatings across a broad temperature range. We focus on investigating four key aspects: (1) the mechanism by which biomimetic textures regulate lubricant storage and release behavior; (2) the antioxidative protection mechanism of B_2O_3/Bi_2O_3 eutectic glass phases on graphite; (3) the synergistic and complementary lubrication mechanisms of the B_2O_3/Bi_2O_3/C ternary system at different temperature segments; and (4) the in-situ formation process and long-term lubrication mechanism of the friction interface glaze layer at extreme high temperatures. This work not only reports composite coatings with low and stable friction coefficients over the wide temperature range of 25–800 °C but also reveals their temperature-dependent intelligent synergistic lubrication mechanism from the perspectives of microstructural evolution and atomic-scale simulation, providing theoretical and experimental foundations for the design of next-generation adaptive self-lubricating coatings for extreme operating conditions.

2. Experimental section

2.1 Preparation of Cr_3C_2-NiCr coating

Cr_3C_2-NiCr coatings with a thickness of 230–280 μm were deposited on 316L stainless steel substrates (Φ25.4 × 6 mm) using a high-velocity oxy-fuel (HVOF) system (GTV K2, Germany). The thermally sprayed powder (−45 +15 μm) was commercially available, and its basic information along with the coating preparation process is shown in part 1 of Fig. 1. The HVOF spraying parameters were as follows: carrier gas flow rate of 9 L/min, powder feed rate of 1.2 r/min, kerosene flow rate of 25 L/min, oxygen flow rate of 890 L/min, combustion ratio of 1.2, and cooling power of 75 kW.

2.2 Laser surface texture of Cr_3C_2-NiCr coating

Biomimetic honeycomb-shaped regular hexagonal textures were fabricated on Cr_3C_2-NiCr coating surfaces using a laser manufacturing system (BLT-S200 LPBF, Xi'an Bright Laser Technologies Co., Ltd., Xi'an, China). The laser textures had a depth of 60–80 μm, a side length of 290 μm, and a center-to-center distance of 600 μm. In laser texturing, all pattern dimensions are based on our prior systematic optimization and literature [27, 28,47, 48]. This architecture ensures effective lubricant storage and supply while providing optimal surface load-bearing capacity. A schematic diagram of

Just Accepted

the laser texturing process is presented in part 2 of Fig. 1. The laser texturing parameters were: laser power of 170 W, scanning speed of 850 mm/s, laser energy density of 0.16 $J \cdot mm^{-2}$, and wavelength of 1000 nm.

2.3 Preparation of $B_2O_3/Bi_2O_3/C$ ternary solid lubricant

The raw powder information for boron oxide (B_2O_3, 99.98%, −3 +1 μm), bismuth oxide (Bi_2O_3, 99.95%, −3 +1 μm), and graphite (C, 99.93%, −3 +1 μm) as well as the composite powder preparation process is illustrated in part 3 of Fig. 1. A planetary ball mill (ND7-04, Nanda Tianzun Electronic Co., Ltd., Nanjing, China) was employed to mechanically mill the 50 wt% B_2O_3–30 wt% Bi_2O_3–20 wt% C composite powder to produce $B_2O_3/Bi_2O_3/C$ composite powder with uniform particle size. The mechanical milling parameters were: rotational speed of 380–420 rpm, milling time of 1–2 h, and weight ratio of balls to powder of 10:1.

2.4 Preparation of composite coating

The preparation process of the composite coatings is depicted in part 4 of Fig. 1. The $B_2O_3/Bi_2O_3/C$ composite lubricant was uniformly coated on the surface of the laser-textured Cr_3C_2-NiCr coatings, followed by vacuum heat treatment of the samples using a vacuum muffle furnace (KSL-1700X, Hefei Kejing Materials Technology Co., Ltd., Anhui, China). The eutectic melting point of B_2O_3/Bi_2O_3 is 620 °C; to ensure complete melting, the actual temperature was set to 800 °C with a holding time of 10 min. In vacuum heat treatment, a 10 min hold is the simplest and most efficient parameter derived from preliminary experiments, enabling thorough melt infiltration in the shortest time. The negative pressure under vacuum was used to fully infiltrate the molten composite lubricant into the textured grooves. Excess lubricant on the surface was gently removed using fine sandpaper, leaving only the filler inside the textures. For simplicity, the unmodified Cr_3C_2-NiCr coating specimen was designated as the "C1" coating, and the composite coating specimen modified by laser texturing and $B_2O_3/Bi_2O_3/C$ ternary solid lubricant was designated as the "C2" coating.

2.5 Tribological test

The tribological properties of the C1 and C2 coatings at different temperature ranges were investigated using a high-temperature rotary friction and wear tester (HT-1000, HSR-2M, Zhongke Kaihua Technology Development Co., Ltd., Lanzhou, China). Alumina (Al_2O_3, Φ6 mm, Ra ≤ 200 nm) balls were used as the counterbody. The tribological test parameters were: normal load of 5 N, rotational speed of 500 r/min,

Just Accepted

friction radius of 5 mm, and test temperatures of 25 °C, 400 °C, and 800 °C. Each temperature constituted one thermal cycle, and the friction duration at each temperature was 10 min. A total of four consecutive wide-temperature-range thermal cycle friction and wear tests were conducted. A programmed temperature-control mode of the high-temperature tribometer was employed, with a heating rate of 10 °C/min; cooling was performed by natural cooling within the furnace at approximately 5 °C/min, with the temperature deviation controlled within ±5 °C throughout, ensuring precise and controllable heating and cooling. After reaching each target temperature, the sample was held isothermally for 10 min to ensure overall thermal equilibrium before initiating the friction test; after completion of the test at a single temperature point, the program ramped to the next temperature point, followed by another 10 min holding period before testing. To ensure the reproducibility of the tribological test results, each test was repeated at least three times under the same parameters, and the average values were reported.

2.6 Characterization

The surface microstructures and elemental distributions of the coating wear tracks were analyzed using a field-emission scanning electron microscope (FE-SEM, Nova Nano-450, FEI, USA) equipped with an energy-dispersive X-ray spectrometer (EDS, XLT TEM-SDD, AMETEK EDAX, USA). The phase compositions of the powders and coatings were characterized using an X-ray diffractometer (XRD, Rigaku Smartlab 9 kW, Japan) with Cu-Kα radiation. The three-dimensional surface morphologies of the coatings were analyzed using a non-contact optical profilometer (ADE Corporation, Massachusetts, USA). The distribution of light elements such as boron on the wear track surfaces was examined using an electron probe microanalyzer (EPMA, JXA-8100, JEOL, Japan). Thin foils for transmission electron microscopy (TEM) observation were prepared using a focused ion beam (FIB, Helios NanoLab 600, FEI Corporation, Hillsboro, Oregon, USA). High-resolution microstructures and elemental distributions of the glaze layers on the wear track surfaces after high-temperature friction were characterized using a TEM (TEM, Talos F200X, FEI, USA) to further elucidate the high-temperature lubrication mechanism.

2.7 Molecular Dynamics Simulations

Non-equilibrium molecular dynamics (NEMD) simulations were performed to investigate the structural evolution of B_2O_3/Bi_2O_3 oxide films under the coupled effects

Just Accepted

of normal pressure, shear, and continuous heating. The simulation system adopted a sandwich structure, consisting of a rigid Cr_3C_2 substrate, a B_2O_3 layer, a Bi_2O_3 layer, and a rigid Al_2O_3 friction counterpart from bottom to top. The simulation box dimensions were set to 79.72 Å × 43.53 Å × 72.54 Å, with a total of 12,361 atoms in the system. Periodic boundary conditions were applied in the x and y directions, while non-periodic boundary conditions were used in the z direction. The x direction was defined as the sliding direction, and the z direction was defined as the normal loading direction. The Cr_3C_2 substrate remained completely fixed throughout the simulation. The Al_2O_3 layer was treated as a rigid friction counterpart, which was only used to apply normal load and shear motion, without considering its internal deformation, wear, or interfacial chemical reactions. The atoms in the B_2O_3/Bi_2O_3 films were treated as mobile atoms participating in the dynamic evolution. The B–Bi–O interactions within the oxide films were described using a combination of the Buckingham potential and long-range Coulomb interactions (detailed parameters are provided in the Supporting Information).

Just Accepted

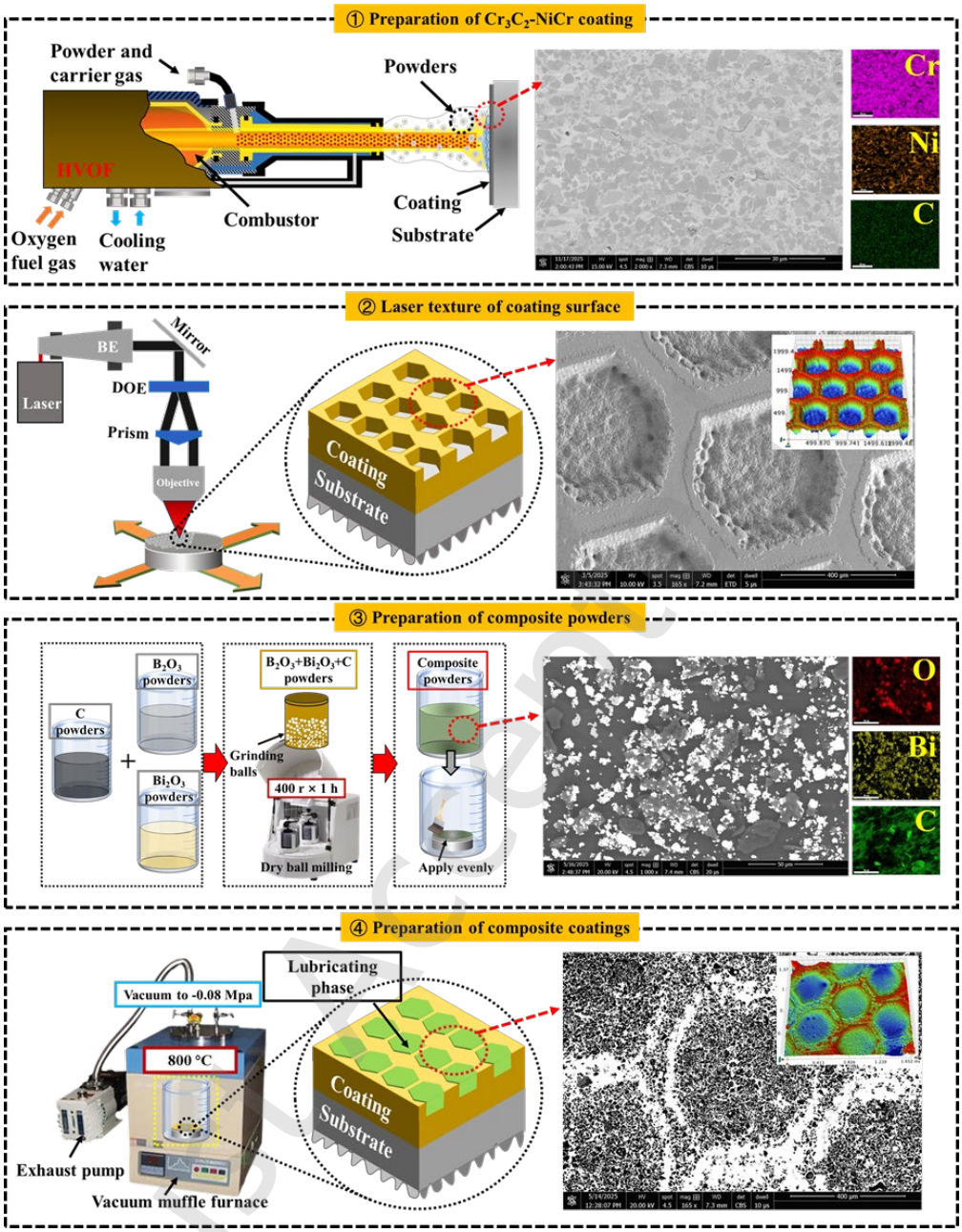


Fig. 1. Schematic illustration of the fabrication process for the Cr_3C_2–NiCr–(B_2O_3/Bi_2O_3/C) composite coating.

3. Results and discussion

3.1 Material Characterization

To elucidate the synergistic effect between the B_2O_3/Bi_2O_3/C ternary composite lubricant and biomimetic honeycomb textures, a systematic set of samples was designed, including the pristine Cr_3C_2-NiCr coating and the Cr_3C_2-NiCr-(B_2O_3/Bi_2O_3/C) composite coating synergistically modified by laser texturing and composite lubricant incorporation. The microstructures and elemental distributions of the samples were further characterized by scanning electron microscopy (SEM) and energy-dispersive X-

ray spectroscopy (EDS).

Part 1 of Fig. 1 presents the SEM micrograph of the as-sprayed Cr_3C_2-NiCr coating fabricated via HVOF technology. The coating exhibits a dense overall structure with uniform elemental distribution and no obvious defects such as pores or cracks (Figs. S1-2, Supporting Information), indicating the high quality of the as-prepared base coating. Part 2 of Fig. 1 shows the SEM morphology of the laser-textured Cr_3C_2-NiCr coating surface. The textured patterns feature regular edges and uniform distribution, with no significant laser-induced defects observed. Part 3 of Fig. 1 displays the SEM micrograph of the B_2O_3/Bi_2O_3/C composite powder. The individual powders have moderate particle sizes and uniform elemental distribution without noticeable agglomeration. Part 4 of Fig. 1 illustrates the surface SEM morphology of the Cr_3C_2-NiCr-(B_2O_3/Bi_2O_3/C) composite coating. The textured grooves on the coating surface are effectively filled with the B_2O_3/Bi_2O_3/C composite lubricant, which is uniformly distributed throughout. The white B_2O_3/Bi_2O_3 phase uniformly encapsulates numerous black graphite particles. These results confirm that the Cr_3C_2-NiCr-(B_2O_3/Bi_2O_3/C) composite coating (designated as the C2 coating) with favorable micro-morphology and structural integrity was successfully fabricated via the combined process of thermal spraying, laser texturing, and vacuum heat treatment.

To further investigate the phase compositions and internal structures of the lubricant material and the C2 coating, X-ray diffraction (XRD) measurements were performed on the Cr_3C_2-NiCr powder, as-sprayed coating, and B_2O_3/Bi_2O_3/C composite lubricant on the C2 coating surface (Figs. 2a-b). More detailed SEM/EDS characterizations were conducted on the surface and cross-section of the C2 coating (Figs. 2c-h). The XRD results reveal that the characteristic peaks of the Cr_3C_2-NiCr powder and coating are well matched, with no obvious phase transformation detected. The characteristic diffraction peaks of the B_2O_3/Bi_2O_3/C composite correspond precisely to the standard PDF card patterns of each individual component. The composite lubricating phase on the C2 coating surface is uniformly distributed, with the white B_2O_3/Bi_2O_3 phase encapsulating the black graphite particles. Numerous submicron- and nanoscale B_2O_3/Bi_2O_3 spherical particles are uniformly adhered to the surfaces of the graphite particles. Cross-sectional SEM observation of the C2 coating reveals the vertical distribution of the B_2O_3/Bi_2O_3/C composite lubricant, where black graphite particles are uniformly embedded in the dense white B_2O_3/Bi_2O_3 matrix,

Just Accepted

consistent with the surface structural state. These results collectively demonstrate that the phase compositions, microstructures, and elemental distributions of both the composite coating and the lubricant powder are satisfactory and consistent with the experimental design expectations.

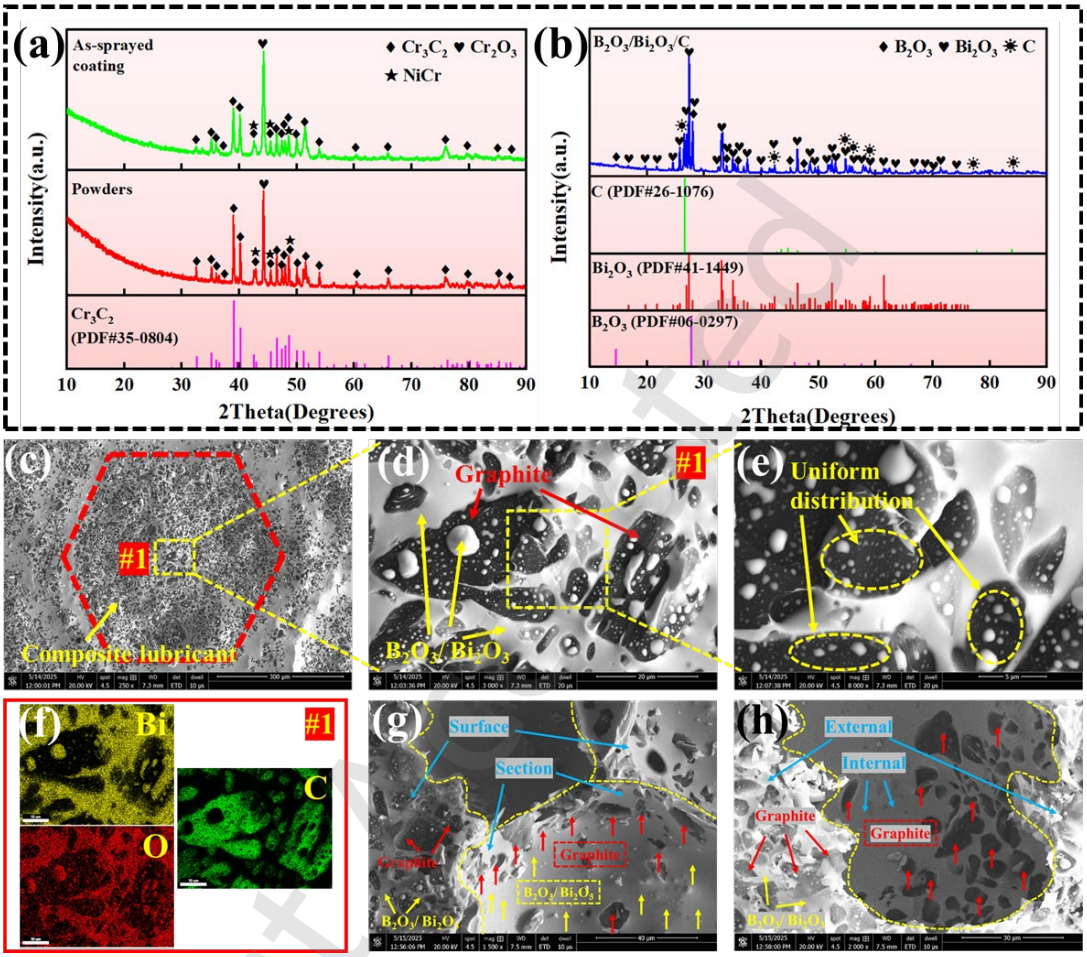


Fig. 2. Micro-morphology, elemental distribution and phase composition of Cr_3C_2-NiCr coating and lubricating materials: (a) XRD patterns of Cr_3C_2-NiCr powders and coating; (b) XRD patterns of lubricating materials; surface (c-e) and fracture surface (g-h) SEM images and EDS-mappings (f) of the composite coating.

3.2 Friction and wear properties

To comprehensively evaluate the tribological potential of the novel composite coating (C2) at different temperature ranges, the tribological properties and temperature dependence of both the C1 and C2 coatings were systematically investigated using a high-temperature friction and wear tester.

Fig. 3 (a) presents the representative coefficient of friction (COF) curves of the C1 coating over 25–800 °C. At 25 °C, the COF increased sharply to approximately 0.8 within a very short time, followed by minor fluctuations and eventually stabilized at

around 0.86. At 400 °C, the COF rose rapidly to approximately 0.6 within 1 min, underwent severe fluctuations, and finally stabilized at about 0.59. At 800 °C, the COF reached a peak value of approximately 0.7 after 1 min of friction, then decreased continuously and stabilized at around 0.51.

Figs. 3 (d–f) show the COF curves of the C2 coating subjected to four consecutive thermal cycles over 25–800 °C. At 25 °C, the COF was lowest in the first cycle, which eventually stabilized at approximately 0.05; with increasing cycle number, the COF gradually increased and plateaued at around 0.11. At 400 °C, the first cycle also showed the lowest COF, stabilizing at approximately 0.12; as the number of cycles increased, the COF rose and plateaued at about 0.17. In contrast, at 800 °C, the first cycle displayed the highest COF, stabilizing at approximately 0.25, and the COF gradually decreased to around 0.1 with increasing cycle number. Fig. 3 (b) presents the statistical bar graph of the average COFs for the C1 and C2 coatings after four thermal cycles over 25–800 °C. The results demonstrate that the average COFs of the C2 coating at 25 °C, 400 °C, and 800 °C were 0.08, 0.14, and 0.12, respectively, corresponding to significant reductions of 90.5%, 75.4%, and 76.9% compared with those of the C1 coating (0.84, 0.57, and 0.52). Fig. 3 (c) presents the statistical bar chart of wear rates for C1 and C2 coatings after four thermal cycles over 25–800 °C. The results show that the wear rates of the C2 coating at 25 °C, 400 °C, and 800 °C are 0.13×10^{-5}, 0.26×10^{-5}, and 0.15×10^{-5} mm³/(N·m), respectively. Compared with the C1 coating (1.59×10^{-5}, 2.58×10^{-5}, and 13.86×10^{-5} mm³/(N·m)), these values are one order of magnitude lower at 25 °C and 400 °C, and two orders of magnitude lower at 800 °C. Comparing the cross-sectional profiles of the wear tracks of C1 and C2 coatings (Figs. 3g–i), the wear depths of the C2 coating at 25 °C, 400 °C, and 800 °C (1.7 μm, 2.8 μm, and 1.9 μm) are significantly shallower than those of the C1 coating (9.2 μm, 11.5 μm, and 40.6 μm).

Collectively, the unmodified C1 coating exhibited no significant self-lubricating properties at any tested temperature. In stark contrast, the C2 coating demonstrated outstanding self-lubricating performance across all temperature ranges. Notably, the COF of the C2 coating exhibited distinct evolution patterns with increasing cycle number at different temperatures: it increased with cycle number at 25 °C and 400 °C, but decreased at 800 °C. In terms of wear rate, the C2 coating exhibits superior wear resistance across all temperature ranges compared with the unmodified C1 coating. This

Just Accepted

observation suggests that the composite lubricating phase on the C2 coating surface operates via different lubrication mechanisms at different temperature ranges, which will be further elucidated in subsequent sections through detailed microstructural analyses of wear track morphologies and complementary characterizations.

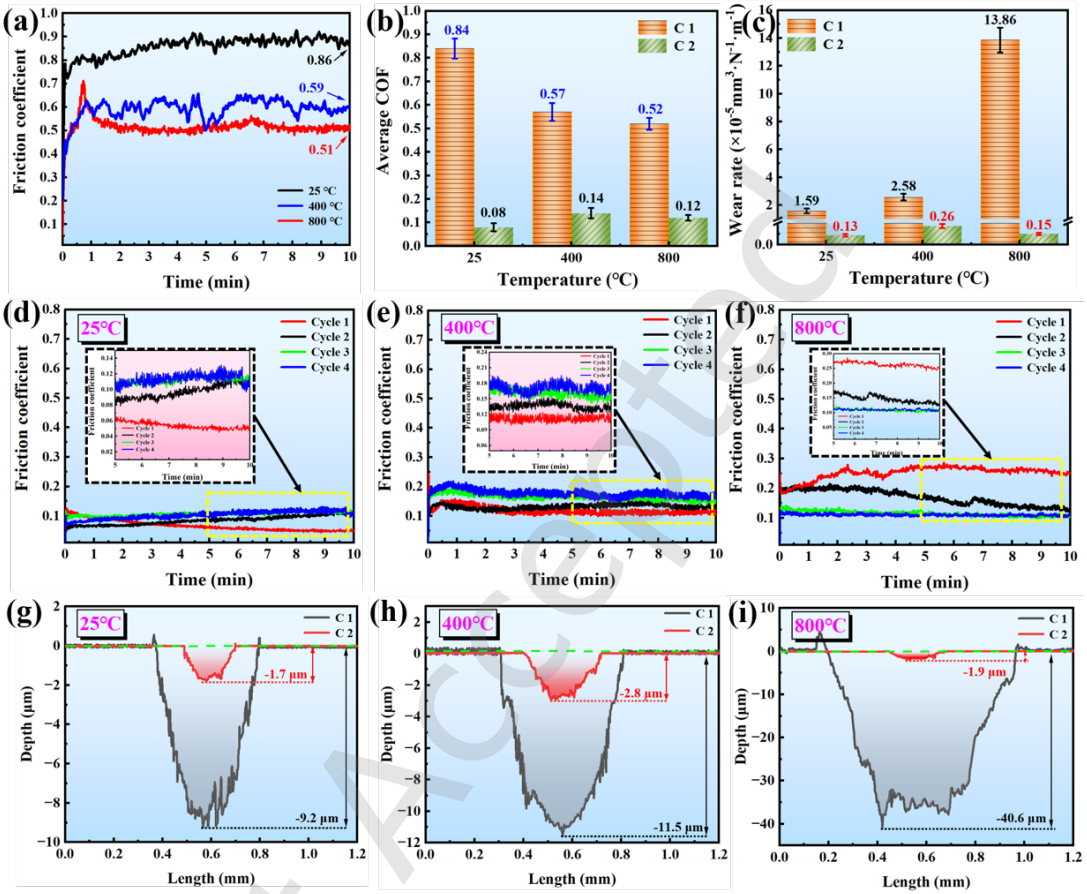


Fig. 3. Wide-temperature tribological behavior: (a) classical COF variation curves of C1 coating at 25–800 °C; (b, c) average COF and wear rate of C1–2 coatings after four thermal cycles at 25–800 °C; classical COF variation curves of C2 coating after four thermal cycles at 25 °C (d), 400 °C (e) and 800 °C (f); wear track cross-sectional profiles of C1–2 coatings after four thermal cycles at 25 °C (g), 400 °C (h) and 800 °C (i).

3.3 Characterization and analysis of wear surfaces

The correlation between microstructural evolution under sliding contact and the temperature-dependent tribological performance of protective coatings has been extensively documented in existing literature [49,50]. Analyses of worn-track microtopography and elemental distribution enable unambiguous identification of temperature-regulated wear behaviors and underlying lubrication mechanisms [51]. The microstructure and elemental distribution of the worn surface of the C2 coating

Just Accepted

after the fourth thermal cycle across 25–800 °C were characterized (Figs. 4-7).

At 25 °C, abundant black graphite domains remain confined within the hexagonal textured cavities of the C2 coating, whereas the non-textured flat regions are covered with continuous white B_2O_3/Bi_2O_3 phase (Figs. 4a-b). High-magnification inspection of localized wear tracks reveals negligible abrasive or adhesive damage; graphite grains are homogeneously encapsulated by the surrounding B_2O_3/Bi_2O_3 matrix, with numerous nanoscale spherical B_2O_3/Bi_2O_3 nanoparticles anchored onto graphite surfaces. Further magnification of graphite-rich domains reveals the inherent lamellar microstructure of pristine graphite (Figs. 4c-f). These morphological observations confirm that most embedded graphite retains its characteristic layered architecture without severe oxidative degradation after three sequential 25–800 °C thermal cycles. Accordingly, room-temperature lubrication is dominated by solid lubrication originating from intact graphite flakes. Combined with the preceding COF evolution curves, the gradual rise in friction coefficient upon repeated thermal cycling originates from progressive consumption of graphite lubricant during intermittent high-temperature exposure. Nevertheless, the enveloping B_2O_3/Bi_2O_3 matrix effectively suppresses graphite high-temperature oxidation, restricting the stabilized COF below 0.12 and verifying the prominent antioxidative capability of B_2O_3/Bi_2O_3.

At 400 °C, distinct black graphite-rich domains persist inside textured grooves despite measurable graphite loss relative to specimens tested at 25 °C, as validated via elemental compositional analysis (Figs. 5a-b). Further magnification of the graphite-rich region on the worn surface reveals a typical layered structure, where numerous graphite particles are encapsulated by the “white armor layer”. Elemental analysis confirms that this layer is a dense antioxidant coating formed by B_2O_3/Bi_2O_3. This protective shield effectively suppresses high-temperature oxidation of the graphite particles (Figs. 5c-e). Nanoscale B_2O_3/Bi_2O_3 nanoparticles adhere densely to graphite surfaces, acting as nanoscale rolling bearings to reduce interfacial friction while blocking high-temperature oxidation (Figs. 5e-g). Figs.5 (h-i) display the morphology of non-textured wear areas, where a protuberance-containing glaze film forms uniformly atop the Cr_3C_2-NiCr substrate. EDS point-scan characterization identifies the protrusive glaze constituents as crystalline Bi_2O_3 and partially molten B_2O_3 nanoparticles. Collectively, synergistic lubrication at 400 °C is jointly governed by layered graphite, discrete nanosized Bi_2O_3 particles and partially softened B_2O_3. Slow

Just Accepted

graphite depletion upon cyclic thermal loading accounts for moderate COF elevation, yet the composite lubricating system confines the steady-state friction coefficient below 0.17.

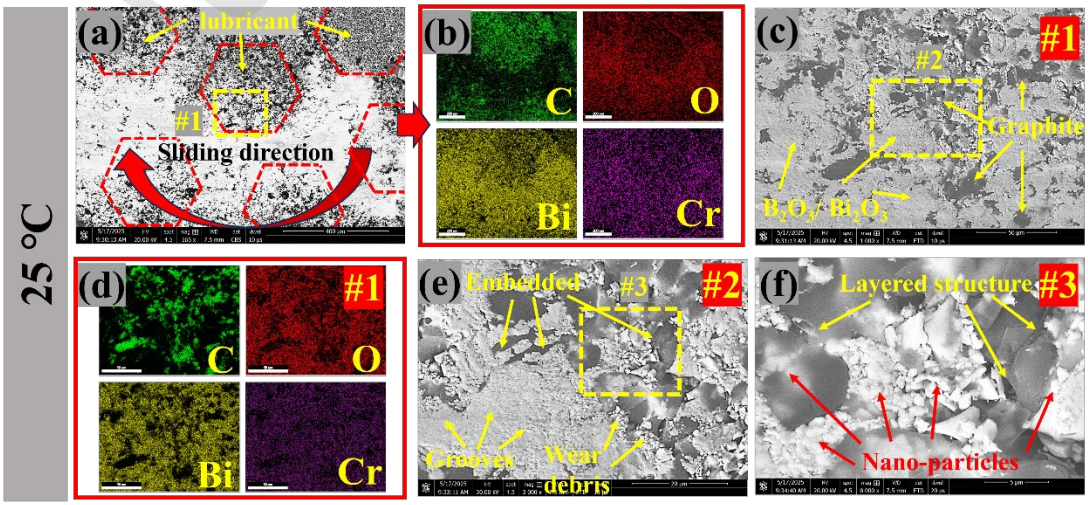
At 800 °C, large continuous black graphite aggregates vanish within hexagonal textured cavities, while discrete fine carbon-rich inclusions are embedded inside non-textured wear zones with evident carbon elemental enrichment (Figs. 6a-b). Local high-magnification views reveal bright protrusive asperities assigned primarily to Bi_2O_3 via elemental identification, and refined black nanoparticles with concentrated carbon signals emerge upon further zooming into dark domains (Figs. 6c-j). Detailed inspection at Site #4 uncovers pronounced morphological divergence of glaze layers between inner and outer wear-track annuli (Figs. 6k-l): the inner ring features elevated Cr signal intensity corresponding to thinner glaze coverage, whereas the outer ring is enriched in C, O and Bi and covered by thicker glaze with denser surface asperities; a sharp dividing line separates these two glaze regimes. EPMA mapping with superior atomic counting precision was implemented to trace the spatial distribution of light B and C elements at high temperature (Fig. 7). EPMA analysis of the unworn surfaces for the C2 coating confirmed a uniform distribution of C and B elements within the hexagonal textured microcavities (Fig. 7a). Following high-temperature tribological testing at 800 °C, distinct boron enrichment was detected in the composite lubricant phase regions inside the wear scar, with pronounced carbon signals observed along the sliding direction of the wear track (Fig. 7b). These findings demonstrate that high-temperature lubrication at 800 °C is dominated by liquid-phase lubrication derived from fused B_2O_3/Bi_2O_3 glaze layers. Original bulk graphite is pulverized into fine particulate fragments under coupled thermal and shear loadings and subsequently trapped within the rigid glaze matrix. The encapsulating B_2O_3/Bi_2O_3 “white armor” concurrently delivers high-temperature fluid lubrication and robust antioxidative protection for embedded carbon. Progressive structural densification of the glaze film occurs with increasing thermal cycles, accompanied by thermally driven migration and aggregation of low-melting-point B_2O_3/Bi_2O_3 toward the sliding interface, ultimately reducing the steady-state COF to ~0.1.

To further quantify the oxidation inhibition effect of B_2O_3/Bi_2O_3 on graphite, EDS elemental quantification and XRD phase characterization were performed on the worn surfaces of the C2 coating at different temperature ranges after four thermal cycles (Fig.

Just Accepted

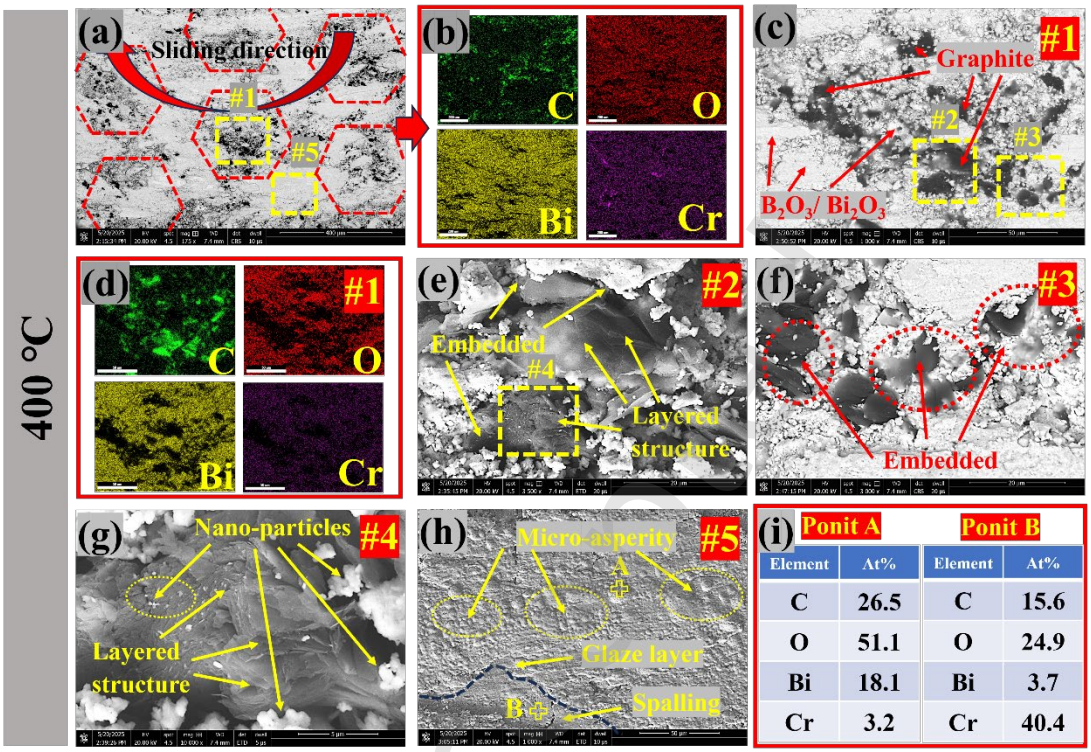
8). After one thermal cycle over 25–800 °C, the C content within the wear track of the C2 coating decreased by only 7.09%, while the O and Bi contents increased by 6.28% and 1.04%, respectively. After four thermal cycles, the C content within the wear track remained as high as 25.74%, with the O and Bi contents increasing to 50.23% and 17.85%, respectively. The EDS results (Fig. 8a) indicate significant inhibition of graphite oxidation at the tribological interface, whereby molten B_2O_3/Bi_2O_3 at elevated temperatures retards oxygen attack. Consistent with this, the XRD results (Fig. 8b) confirm that graphite diffraction peaks remain detectable on the worn surface of the C2 coating after four thermal cycles, demonstrating that the graphite was not completely oxidized under the protection of B_2O_3/Bi_2O_3. Furthermore, the XRD patterns of the wear tracks show that at 25 °C, graphite diffraction peaks dominate; at 400 °C, the pattern is dominated by graphite and fine-grained B_2O_3/Bi_2O_3 particles, along with a small amount of Al_2O_3 debris from the counterface ball; and at 800 °C, the main B_2O_3/Bi_2O_3 peaks appear as a broad diffuse hump, characteristic of an amorphous state, accompanied by numerous fine-grained diffraction peaks of Al_2O_3, Cr_2O_3, and NiO. These results are fully consistent with the SEM/EDS findings.

In summary, the C2 coating retains outstanding self-lubricating performance after four successive 25–800 °C thermal friction cycles, which originates fundamentally from the synergistic coupling between biomimetic laser textures and the B_2O_3/Bi_2O_3/C ternary lubricant system that sustains efficient interfacial lubrication across wide temperature gradients. Most notably, the B_2O_3/Bi_2O_3 dual oxide matrix displays exceptional high-temperature antioxidation capacity to retard thermo-oxidative degradation of graphite, enabling persistent solid-lubricating functionality of carbon after repeated wide-temperature cyclic service.



Just Accepted

Fig. 4. SEM morphologies and EDS of the worn surfaces for C2 coating at 25 ℃: (a) SEM image; (b, d) corresponding EDS-mappings of (a, c); (c, e, and f) corresponding magnified SEM images of (a).



Element	At%	Element	At%
C	26.5	C	15.6
O	51.1	O	24.9
Bi	18.1	Bi	3.7
Cr	3.2	Cr	40.4

Fig. 5. SEM morphologies and EDS of the worn surfaces for C2 coating at 400 ℃: (a) SEM image; (b, d) corresponding EDS-mappings of (a, c); (c, e-h) corresponding magnified SEM images of (a); (i) corresponding EDS-point of (h).

Just Accepted

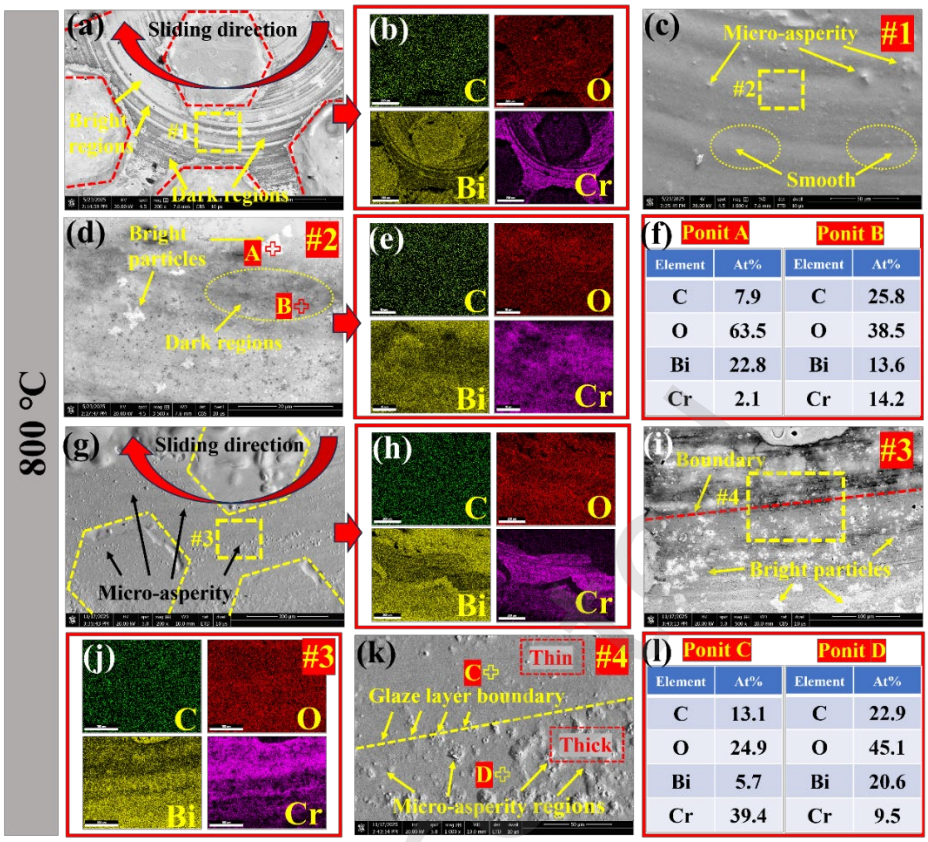


Fig. 6. SEM morphologies and EDS of the worn surfaces for C2 coating at 800 ℃: (a) SEM image; (b, e) corresponding EDS-mappings of (a, d); (c-d) corresponding magnified SEM images of (a); (f) corresponding EDS-point of (d); (h, j) corresponding EDS-mappings of (g, i); (i, k) corresponding magnified SEM images of (g); (l) corresponding EDS-point of (k).

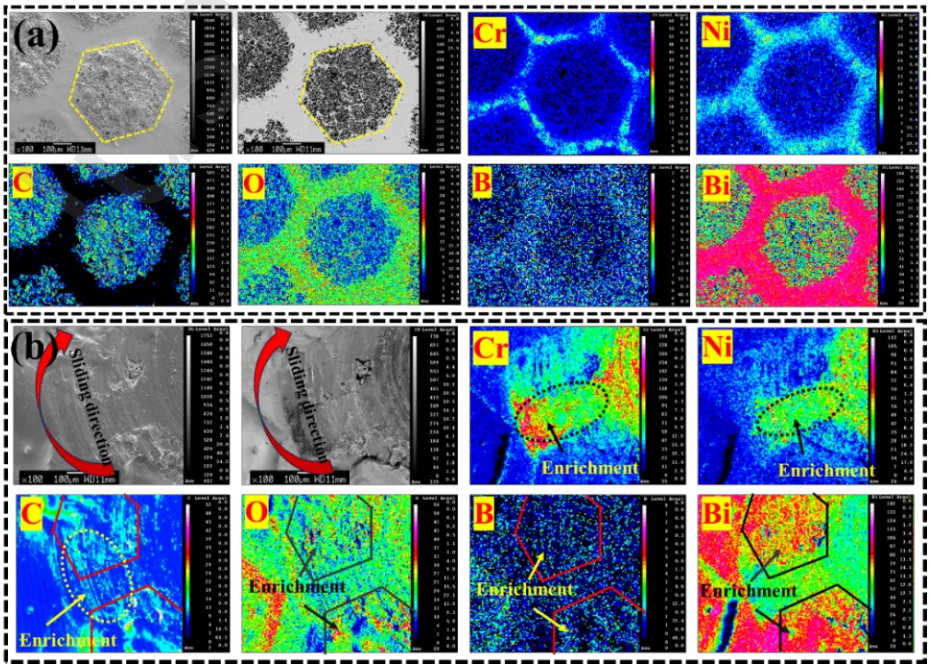


Fig. 7. EPMA elemental maps of the C2 coating after testing at 800 °C: (a) unworn surface; (b) worn surface.

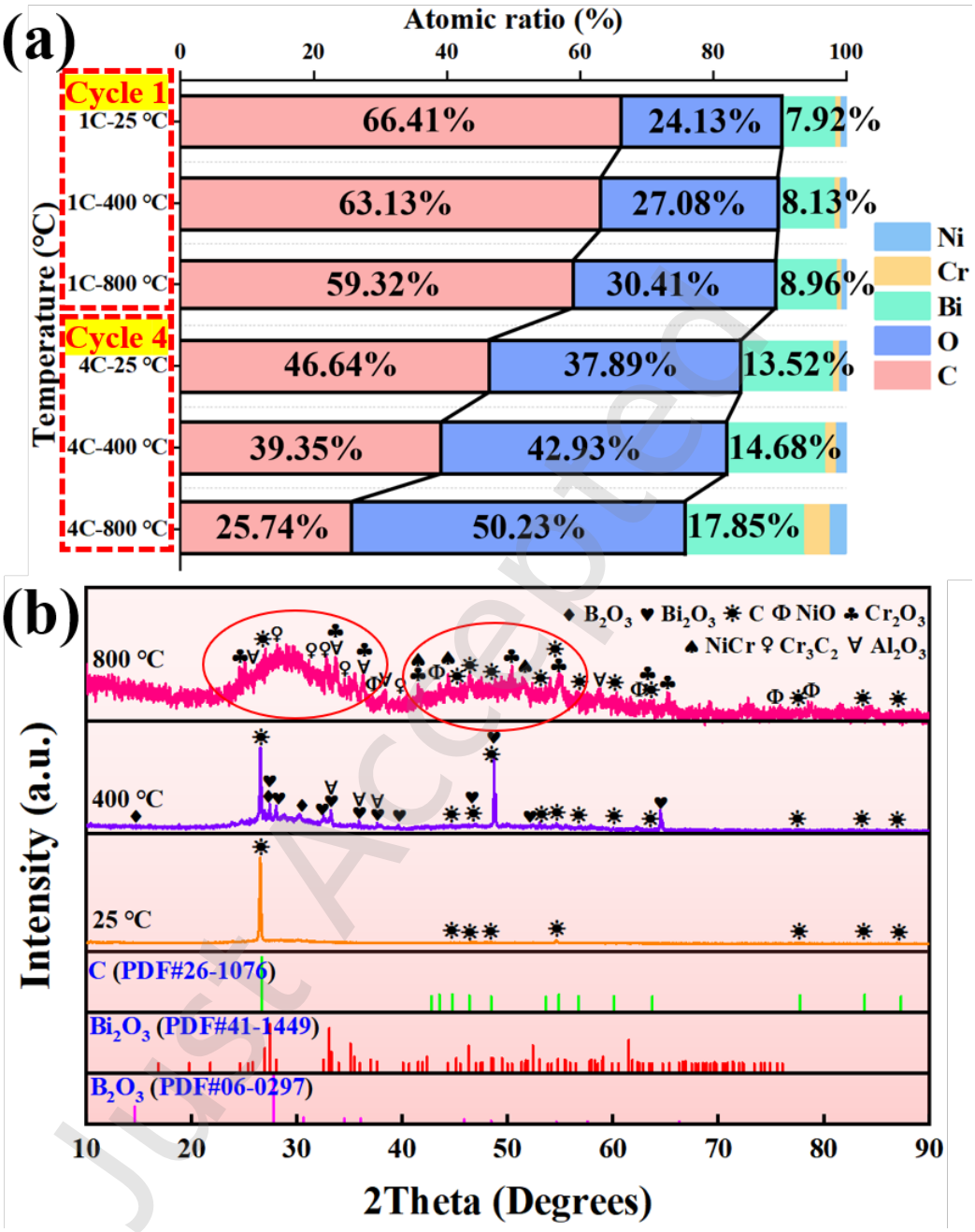


Fig. 8. EDS elemental composition (a) and XRD patterns (b) of the worn surfaces for C2 coating after four thermal cycles at 25–800 °C.

3.4 Microstructure and composition of the glaze layer

To further elucidate the high-temperature lubrication mechanism of the C2 coating, transmission electron microscopy (TEM) analyses were performed to investigate the atomic-scale microstructure and phase composition of the glaze layer formed on the wear scar surface at 800 °C (Fig. S3, Supporting Information).

Just Accepted

Fig. 9 presents the TEM microstructures and elemental distributions of the glaze layer on the C2 coating wear scar after testing at 800 °C. The glaze layer exhibits a well-defined bilayer architecture with a sharp interface, consisting of an outer glaze layer (~600 nm) and an inner glaze layer (220–890 nm), with an additional ~100 nm-thick continuous amorphous layer at the outermost surface of the outer glaze layer (Fig. 9a). TEM-EDS elemental mapping reveals that the outermost amorphous layer is predominantly composed of B_2O_3/Bi_2O_3, which likely originates from combined effect of shear-induced amorphization and glass-forming ability that preserves the liquid-like disordered atomic arrangement to form an amorphous glassy phase [50-53]; this structural origin will be further validated by molecular dynamics simulations in subsequent sections.

The outer glaze layer is primarily constructed from an amorphous B_2O_3/Bi_2O_3 matrix embedding numerous crystalline grains with diverse morphologies, which are mainly enriched in O, Ni and C, with minor amounts of Cr and Al. In contrast, the inner glaze layer consists of finer nanocrystalline grains and a small fraction of amorphous phase identical in composition to that in the outer glaze layer (B_2O_3/Bi_2O_3), while the crystalline grains are dominated by O, Ni and Cr. Fast Fourier transform (FFT) analysis of the interfacial region between the inner and outer glaze layers confirms the coexistence of multiple crystalline phases within the diffraction rings. High-magnification observation of the interfacial region (Fig. 9b) shows that the crystalline grains in the outer glaze layer are predominantly blocky (red circles, Cr-enriched) and rod-like (yellow circles, Ni-enriched), whereas the inner glaze layer is dominated by finer granular nanocrystals (orange circles, Ni-enriched; red circles, Cr-enriched).

High-resolution transmission electron microscopy (HR-TEM) and corresponding FFT analyses were conducted to further characterize the atomic structure and phase identification of the glaze layer (Fig. 10). The top region of the outer glaze layer is a dense, defect-free amorphous film. Representative blocky and rod-like crystalline grains within the outer glaze layer were analyzed by BF-TEM and HR-TEM (Figs. 10a–c), followed by FFT transformation of the HR-TEM lattice images (Figs. 10d–h). Interplanar spacing calibration (Fig. 10i) unambiguously identifies the Al- and O-enriched blocky grains as α-Al_2O_3, the Cr- and O-enriched blocky grains as Cr_2O_3, and the Ni- and O-enriched rod-like grains as NiO. Similarly, BF-TEM, HR-TEM and FFT analyses of the granular nanocrystals in the inner glaze layer (Figs. 10j–q) confirm their

Just Accepted

phase compositions via interplanar spacing matching (Fig. 10r): the Cr- and O-enriched grains are Cr_2O_3, and the Ni- and O-enriched grains are NiO.

Collectively, the glaze layer formed on the C2 coating wear scar at 800 °C exhibits a functionally graded bilayer structure. The outer glaze layer consists of a continuous amorphous B_2O_3/Bi_2O_3 matrix embedding a small number of large-sized blocky Al_2O_3 and Cr_2O_3 grains, along with abundant rod-like NiO grains. The inner glaze layer contains a minor fraction of amorphous B_2O_3/Bi_2O_3 and a large quantity of fine granular Cr_2O_3 and NiO nanocrystals. The amorphous B_2O_3/Bi_2O_3 in the outer glaze layer exists as a viscous fluid glassy state at the 800 °C sliding interface, which serves dual critical functions: first, it provides excellent liquid-phase lubrication by reducing interfacial shear strength; second, it effectively encapsulates large wear debris particles originating from both the Al_2O_3 counterpart ball and the coating substrate, thereby suppressing abrasive wear. Concurrently, the formation of a transfer film from the counterpart material within the outer glaze layer provides mechanical support for the continuous fluid lubricating film. The abundant fine-sized Cr_2O_3 and NiO nanocrystals in the inner glaze layer are formed by the repeated compaction and subsidence of large grains at the sliding interface under cyclic shear loading. The Gibbs free energy changes (ΔG) for reactions (1) and (2) are −287 KJ/mol and −567 KJ/mol, respectively; both ΔG values are significantly negative [54], confirming that both reactions are thermodynamically spontaneous. The above results indicate that a series of tribochemical reactions occurred at the friction interface, which is an inevitable consequence of the coupled thermo-mechanical action at high-temperature frictional contacts. These nanocrystals exhibit two essential protective roles: first, their excellent high-temperature oxidation resistance forms a dense barrier that protects the underlying Cr_3C_2-NiCr coating substrate from oxidative degradation; second, the Cr_2O_3-dominated fine nanocrystals act as a hard reinforcing skeleton to effectively support the outer fluid lubricating film and prevent its excessive extrusion under contact pressure. In brief, the dual glaze layers provide a quadruple protective effect: the outer glaze layer dominates liquid lubrication and wear-debris encapsulation, while the inner glaze layer primarily functions as an oxidation barrier and structural support.

$$2Ni + O_2 \rightarrow 2NiO \qquad \Delta G=-287KJ/mol \tag{1}$$

$$4/3Cr + O_2 \rightarrow 2/3Cr_2O_3 \qquad \Delta G=-567KJ/mol \tag{2}$$

Just Accepted

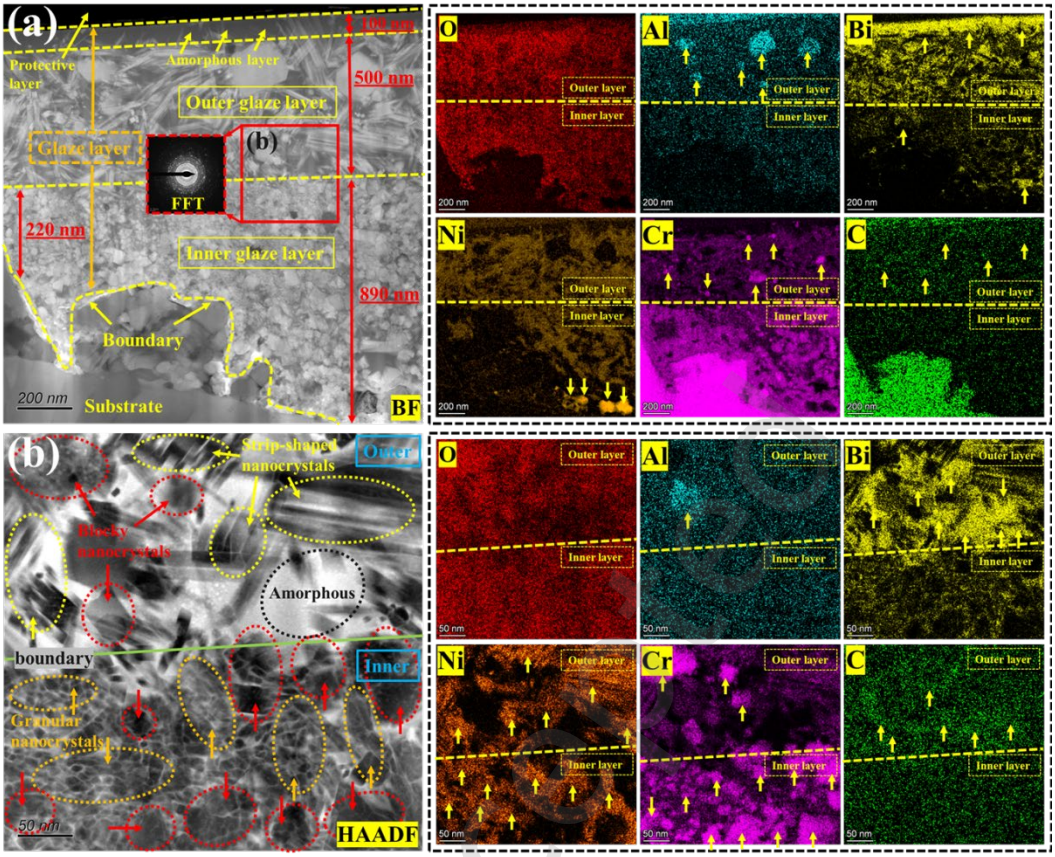


Fig. 9. Cross-sectional TEM images of the worn surface of the C2 coating after testing at 800 °C: (a) bright-field (BF) TEM image and corresponding EDS elemental maps of the FIB-prepared thin foil; (b) corresponding HAADF-TEM image and EDS elemental maps of panel (a).

Just Accepted

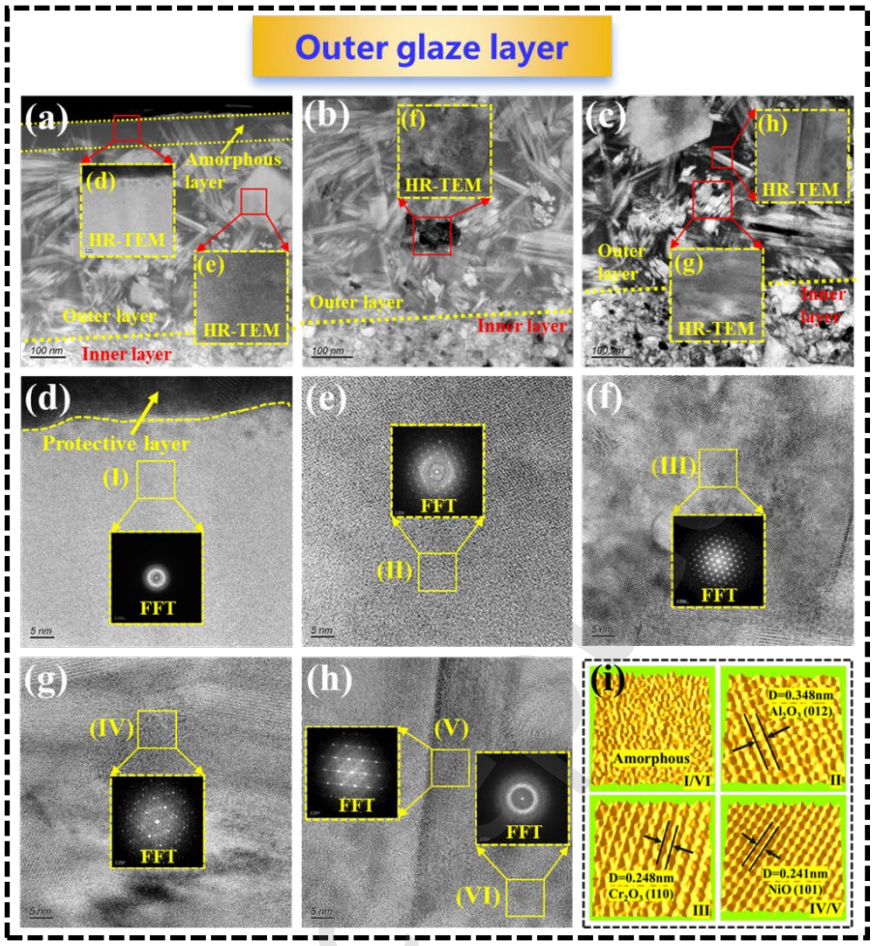

Outer glaze layer
(a)
(d)
HR-TEM
Amorphous layer
(e)
HR-TEM
Outer layer
Inner layer
100 nm
(b)
(f)
HR-TEM
Outer layer
Inner layer
100 nm
(c)
(h)
HR-TEM
Outer layer
(g)
HR-TEM
Inner layer
100 nm
(d)
Protective layer
(I)
FFT
5 nm
(e)
FFT
(II)
5 nm
(f)
(III)
FFT
5 nm
(g)
(IV)
FFT
5 nm
(h)
(V)
FFT
FFT
(VI)
5 nm
(i)
Amorphous
I/VI
D=0.348nm
Al2O3 (012)
II
D=0.248nm
Cr2O3 (110)
III
D=0.241nm
NiO (101)
IV/V
Inner glaze layer
(j)
(m)
HR-TEM
Outer layer
Inner layer
100 nm
(k)
Inner layer
(o)
HR-TEM
(n)
HR-TEM
100 nm
(l)
(p)
HR-TEM
(q)
HR-TEM
100 nm
(m)
FFT
(I)
5 nm
(n)
FFT
(II)
5 nm
(o)
(III)
FFT
5 nm
(p)
FFT
(IV)
(V)
FFT
5 nm
(q)
(VI)
(VII)
5 nm
(r)
D=0.267nm
Cr2O3 (104)
I
D=0.363nm
Cr2O3 (012)
II/VII
D=0.209nm
NiO (012)
III/IV
Amorphous
V/VI

Fig. 10. Cross-sectional TEM images of the glaze layer: (a–c) BF-TEM images of the outer glaze layer; (d–h) corresponding high-resolution TEM (HR-TEM) images and fast Fourier transform (FFT) patterns of the regions marked in (a–c); (i) 3D atomic arrangement order factor (AOGF) profiles of panels (d–h); (j–l) BF-TEM images of the inner glaze layer; (m–q) corresponding HR-TEM images and FFT patterns of the regions marked in (j–l); (r) 3D AOGF profiles of panels (m–q).

3.5 Theoretical Simulations

Building on the preceding structural and compositional analyses of the lubricating glaze layer formed on the C2 composite coating wear scar at 800 °C, we identified that the B_2O_3/Bi_2O_3 film responsible for the dominant lubrication effect at the high-temperature sliding interface exists in an amorphous state. To further elucidate the structural response and lubrication mechanism of the amorphous B_2O_3/Bi_2O_3 film during high-temperature sliding, a sandwich-type friction model was constructed and non-equilibrium molecular dynamics (NEMD) simulations were performed. This computational approach enables direct correlation between local structural rearrangements and film softening during tribological processes. Moreover, the temperature range in the MD simulations (298–1400 K) covers the crystalline-to-amorphous transition points of the low-melting-point oxides B_2O_3 (~723 K) and Bi_2O_3 (~1098 K), enabling a clearer depiction of the complete structural evolution of the lubricating layer. This temperature setting serves as an accelerated sampling strategy to rapidly capture molecular transformation pathways, rather than replicating the exact wide-temperature friction test conditions (298–1073 K).

Fig. 11 (a) presents the atomic configuration evolution of the B_2O_3/Bi_2O_3 film at different stages (Stages 1–4) of the simulation. At Stage 1 (298 K, ambient temperature), the B_2O_3 and Bi_2O_3 molecular layers at the sliding interface exhibit ordered arrangement with a sharp interlayer interface, indicating a stable crystalline state. At Stage 2 (700 K), under the combined effects of elevated temperature and continuous frictional shear, the B_2O_3 molecular layer undergoes a transition to a disordered state first, while the Bi_2O_3 molecular layer retains its intact crystalline structure. At Stage 3 (1100 K), the B_2O_3 molecules are in a highly disordered state, and the Bi_2O_3 layer initiates structural rearrangement and gradually transforms into a disordered state. The original B_2O_3/Bi_2O_3 interface becomes progressively blurred, with B, Bi, and O atoms intermingling at the interface. At Stage 4 (1400 K), both the B_2O_3 and Bi_2O_3 molecular

Just Accepted

layers are in a highly disordered state, with the original crystalline structure completely lost and molecules misaligned. At this point, the B_2O_3 and Bi_2O_3 molecular layers at the sliding interface have completed the transition from crystalline solid to amorphous liquid. Under the combined effects of 1400 K high temperature and frictional heating, B_2O_3 and Bi_2O_3 are fully transformed into a liquid state, forming a continuous B-Bi-O mixed oxide film that exerts fluid lubrication at the sliding interface. The real-time dynamic evolution process of the B_2O_3/Bi_2O_3 molecular layers is provided in Movie S1 (Supporting Information).

The radial distribution function (RDF) curves in Fig. 11(b) further validate the aforementioned structural evolution process. At 298 K, the first peaks of the RDF curves for all atomic pairs are relatively sharp and exhibit distinct oscillations over a large r range, indicating significant short-range order and medium-range structural correlation in the system. Upon heating to 700 K, the RDF peaks associated with B_2O_3 begin to decrease in intensity and broaden, reflecting relaxation and rearrangement of the B-O network structure and indicating that B_2O_3 loses partial structural rigidity first. At approximately 1100 K, the RDF peaks further weaken, and the Bi-O local structure also exhibits significant perturbations, indicating that Bi_2O_3 begins to participate in atomic rearrangement and interfacial mixing. At 1400 K, all RDF peaks are globally reduced and significantly broadened, with the long-range region approaching unity, indicating that the original medium-range ordered structure has essentially disappeared and the system has formed a highly disordered B-Bi-O mixed structure. Collectively, the configuration evolution and RDF results are mutually consistent and collectively demonstrate that the oxide film undergoes a transition from a low-temperature solid-state layered structure to a high-temperature liquid/liquid-like mixed lubricating film, and this structural transformation directly governs the tribological response.

Figs. 11 (c1–3) present the simulated evolution curves of friction force, normal force, and friction coefficient for the system over the temperature range of 298–1400 K. Correlating these results with the temperature-dependent structural changes of the B_2O_3/Bi_2O_3 film shown in Fig. 11 (a): in the temperature range of 298–900 K, the friction force and friction coefficient exhibit a sharp increasing trend, and the normal force also undergoes severe fluctuations, showing a strong correlation with the variation of friction force. During this stage, Bi_2O_3 remains in the solid state, and B_2O_3 has just entered the semi-molten state. The film exhibits high structural rigidity at this point,

Just Accepted

and applied shear tends to induce local stress accumulation in the contact region, resulting in poor lubrication performance of the tribological system. In the temperature range of 900–1300 K, the friction force, friction coefficient, and normal force all show a sharp decreasing trend. At this point, B_2O_3 has completely transformed from solid to liquid, while Bi_2O_3 is gradually transitioning from the semi-molten state to the liquid state. The relaxation of the B_2O_3/Bi_2O_3 network structure reduces the shear stiffness of the film, transforming it from a solid load-bearing component to a soft phase that readily undergoes atomic rearrangement and shear deformation. This soft layer forms an initial low-shear-strength channel between the friction pairs, allowing part of the tangential stress to be dissipated through intra-film structural rearrangement and local flow, leading to progressively improved lubrication performance of the tribological system. In the temperature range of 1300–1400 K, the friction force, friction coefficient, and normal force all remain at low and stable levels. At this stage, both B_2O_3 and Bi_2O_3 are fully transformed into the liquid state. The prior softening of B_2O_3 provides structural space for the rearrangement of Bi_2O_3, while continuous shear further promotes interdiffusion of interfacial atoms, extending the shear stress distribution from the local soft layer to the interior of the thicker oxide film. Meanwhile, the liquid film exhibits high atomic mobility along the x-direction (sliding direction) and can accommodate applied shear through intra-film viscous flow and structural rearrangement, effectively reducing frictional resistance and demonstrating excellent high-temperature lubrication performance. These results demonstrate that the evolution trends of friction force, normal force, and friction coefficient in the tribological system are strongly correlated with the structural state of the B_2O_3 and Bi_2O_3 molecular layers at the sliding interface, and the film state directly governs the high-temperature tribological performance of the system.

In summary, these findings further confirm that the B_2O_3/Bi_2O_3 at the sliding interface undergoes a transition from crystalline solid to amorphous liquid under the combined effects of high temperature and continuous frictional shear, which is in excellent agreement with our previous TEM experimental results of the lubricating glaze layer. The liquid/liquid-like B-Bi-O lubricating film at the high-temperature sliding interface dissipates applied shear and distributes normal load through a combination of intra-film viscous flow, atomic diffusion, structural rearrangement, and stress homogenization, further reducing the friction coefficient of the composite

Just Accepted

lubrication system and thereby contributing to the stable high-temperature lubrication of the coating. More detailed information regarding the parameter settings of the MD simulations is provided in the Supporting Information.

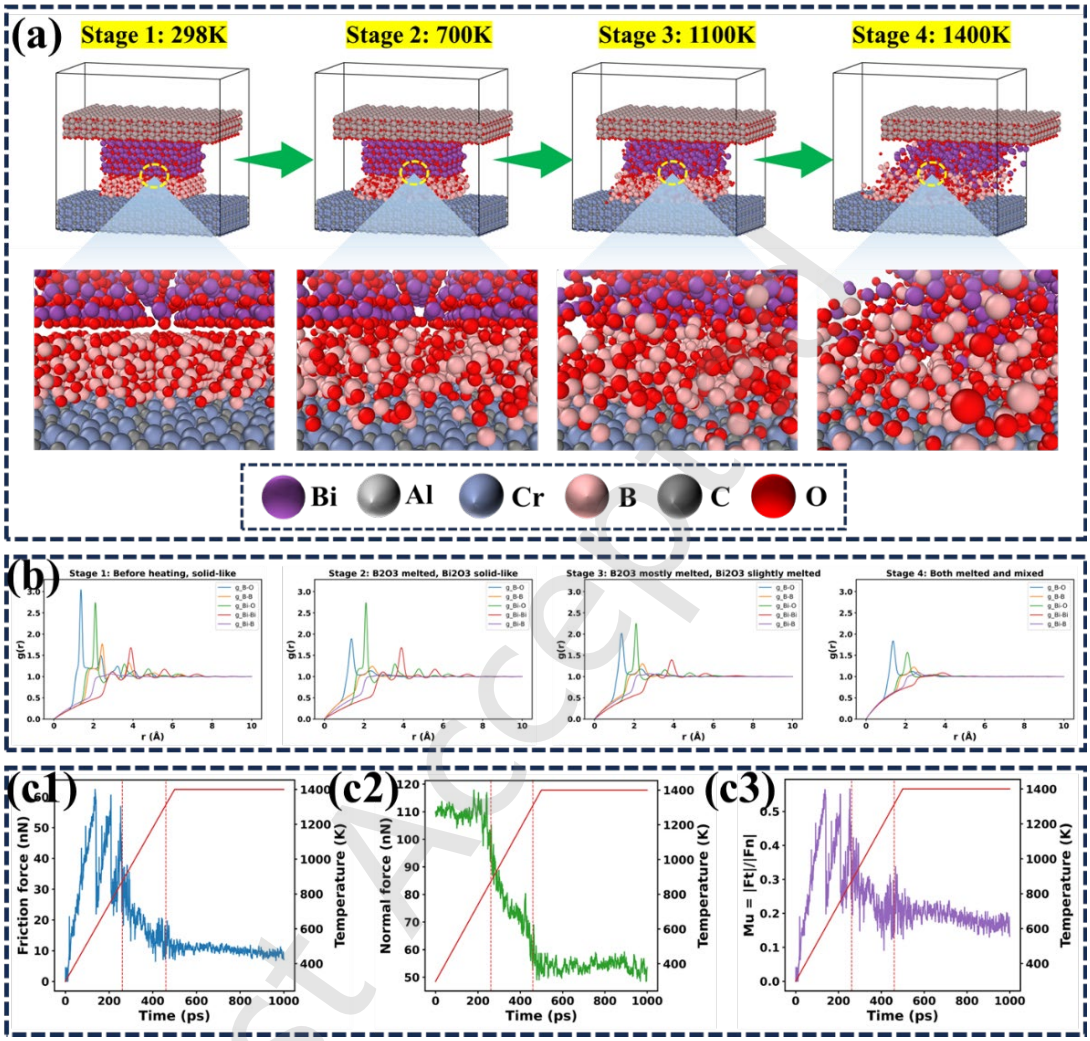


Fig. 11. Non-equilibrium molecular dynamics (NEMD) simulation analysis of the Cr_3C_2–Al_2O_3 friction system: (a) atomic configurations of the B_2O_3/Bi_2O_3 film at different temperature stages; (b) radial distribution functions (RDFs) of the B_2O_3/Bi_2O_3 film at different temperature stages; (c) evolution of the friction force (c1), normal force (c2), and friction coefficient (c3) in the system at different temperatures.

3.6 Synergistic lubrication mechanism

To further elucidate the temperature-dependent synergistic lubrication mechanism of the composite coating over the wide temperature range of 25–800 °C, a schematic illustration of the lubrication mechanisms operating at different temperature segments is presented in Fig. 12. The friction-reducing and lubrication mechanisms at each

temperature regime are detailed as follows:

(1) Room Temperature (25 °C): Micropore Storage-Dominated Lubrication via Graphite Interlayer Sliding

The micropores fabricated by laser texturing on the C2 coating surface function as stable micro/nanoscale lubricant reservoirs. During room-temperature sliding, graphite particles within the micropores are continuously extruded and released to the frictional contact interface, forming a continuous and dense graphite transfer film through the characteristic interlayer van der Waals sliding of graphite. This transfer film converts the direct contact between the hard Cr_3C_2-NiCr coating and the counterpart into low-shear-force sliding between graphite layers, which is the core reason for the ultra-low COF of 0.08 at room temperature. Additionally, nanoscale plastic B_2O_3/Bi_2O_3 particles provide supplementary friction-reducing effects.

(2) Medium Temperature (400 °C): Multiphase Synergistic Lubrication with Antioxidation Barrier Protection

At this temperature regime, which enters the critical oxidation range of graphite, partial surface graphite begins to undergo oxidation reactions. However, the B_2O_3/Bi_2O_3 composite phase preferentially forms a dense antioxidation barrier film that encapsulates and protects the vast majority of graphite particles within the micropores, allowing graphite interlayer sliding lubrication to remain dominant. Concurrently, nanoscale Bi_2O_3 particles generated at the friction interface exert a micro-ball rolling effect, converting partial sliding friction into rolling friction; the semi-molten B_2O_3 forms a viscoplastic lubricating film that fills interfacial micro-pits and reduces shear strength. The three lubricating phases exhibit a well-coordinated synergistic effect, forming a multiphase synergistic lubrication system characterized by "graphite-dominated lubrication + nanoparticle rolling + glassy phase viscoplastic lubrication", which stabilizes the medium-temperature COF at 0.14.

(3) High Temperature (800 °C): Dual-Glaze-Layer Synergistic Lubrication with Quadruple Functional Partition Protection

At high temperatures, most large graphite particles on the coating surface are consumed by oxidation. However, a bilayer-structured "white armor" glaze layer with quadruple protective functions is in-situ formed at the friction interface, realizing a mechanism transition from "solid lubricant lubrication" to "in-situ reacted glaze layer self-lubrication". This transition causes the high-temperature COF to continuously

Just Accepted

decrease to approximately 0.1 with increasing friction cycles:

Outer glaze layer: Predominantly composed of amorphous B_2O_3/Bi_2O_3, which exists in a liquid state at high temperatures. On one hand, it provides high-temperature fluid lubrication; on the other hand, it acts as a wear debris entrapment and encapsulation layer, sequestering hard wear debris generated from both the coating and the counterpart ball to minimize abrasive wear. Meanwhile, the transfer film derived from the counterpart material effectively supports the fluid lubricating film.

Inner glaze layer: Consists of Cr_2O_3 and NiO nanocrystals with a minor fraction of amorphous B_2O_3/Bi_2O_3, forming a dense nanocrystalline composite layer through repeated compaction and subsidence of large grains during friction. It serves dual critical functions: as a high-temperature antioxidation barrier layer protecting the underlying Cr_3C_2-NiCr coating substrate from oxidative degradation, and as a rigid supporting skeleton preventing excessive extrusion and rupture of the liquid lubricating film in the outer glaze layer.

This mechanism achieves long-term friction reduction and protection under extreme temperatures through the quadruple coupling effects of liquid film lubrication, wear debris encapsulation, oxidation blocking, and structural support.

In summary, the composite coating exhibits an excellent stage-dependent synergistic lubrication mechanism that evolves continuously with increasing friction temperature. The solid lubrication of graphite gradually diminishes, but the molten B_2O_3/Bi_2O_3 effectively inhibits graphite oxidation, thereby enhancing its lubrication utilization during repeated thermal cycles. In contrast, the high-temperature lubricating effect of the oxide glaze layer rich in B/Bi/Cr/Ni/Al progressively strengthens, forming a dual glaze layer with quadruple protection at 800 °C and providing superior high-temperature lubrication.

Just Accepted

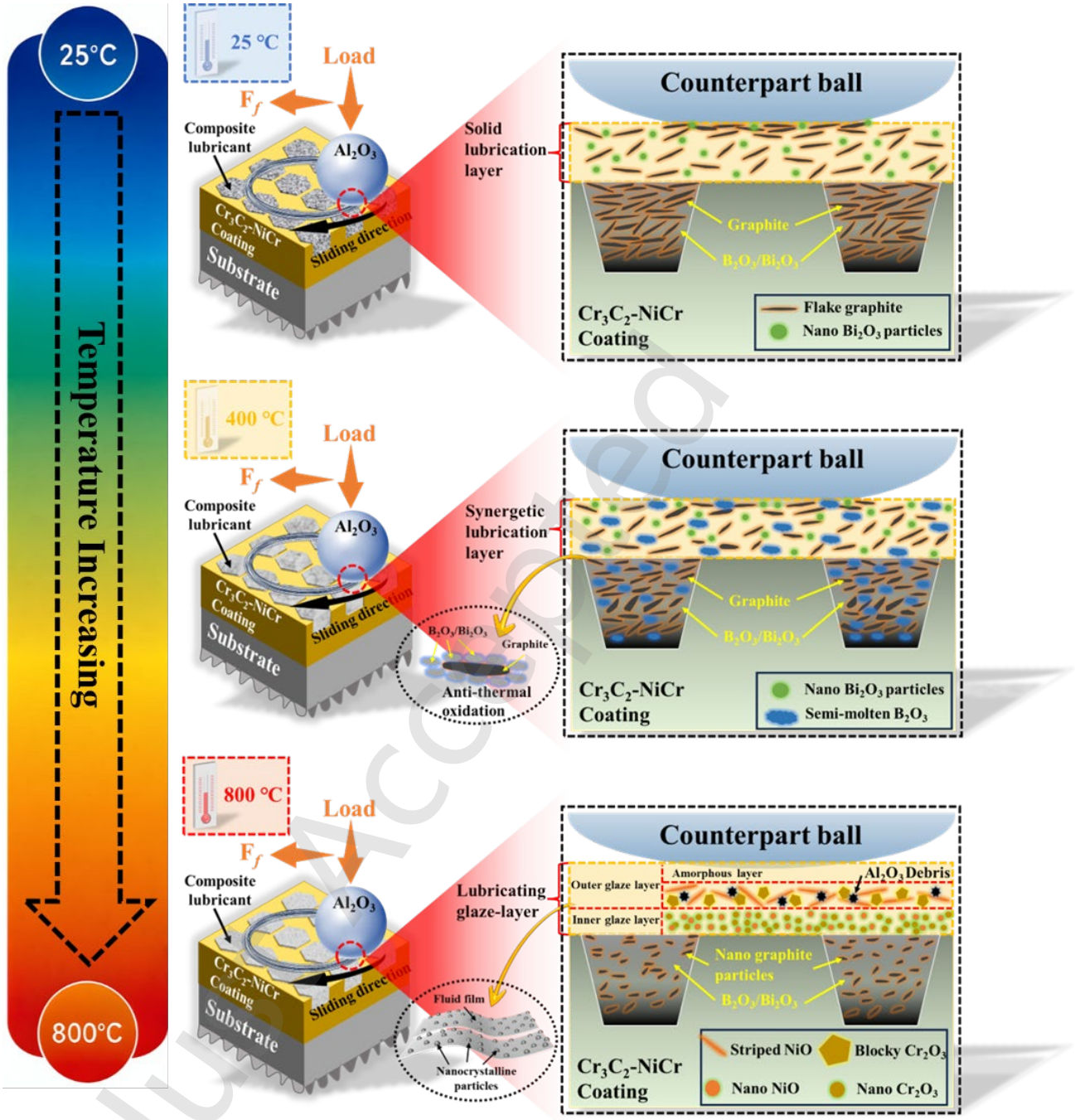


Fig. 12. Schematic illustration of the synergistic self-lubrication mechanism of the C2 coating at 25 °C, 400 °C, and 800 °C.

4. Conclusions

To address the inherent deficiency in self-lubricating performance of conventional Cr_3C_2-NiCr coatings over a wide temperature range, this study innovatively integrated HVOF spraying, honeycomb-shaped laser texturing, and vacuum negative pressure heat treatment into a hybrid fabrication process to develop Cr_3C_2-NiCr-(B_2O_3/Bi_2O_3/C) composite self-lubricating coatings. Systematic investigations including

microstructural characterization, multi-temperature tribological testing, and lubrication mechanism analysis were performed, combined with molecular dynamics simulations to validate the evolution of high-temperature lubricating phases. This work provides both theoretical support and innovative insights for the design of high-performance wide-temperature-range self-lubricating coatings under extreme operating conditions. The main conclusions are summarized as follows:

(1) Biomimetic honeycomb-shaped hexagonal micropores were fabricated on Cr_3C_2-NiCr coating surfaces via laser texturing to serve as lubricant reservoirs, and uniform and dense infiltration of the $B_2O_3/Bi_2O_3/C$ composite lubricant was achieved through subsequent vacuum heat treatment. This design provided a stable storage foundation and controlled lubricant release capability for the frictional interface across wide temperature ranges. The as-fabricated Cr_3C_2-NiCr-($B_2O_3/Bi_2O_3/C$) composite coatings exhibited stable phase compositions and homogeneous elemental distribution.

(2) The composite coatings achieved average COFs of 0.08, 0.14, and 0.12 at 25 °C, 400 °C, and 800 °C, respectively, representing significant reductions of 90.5%, 75.4%, and 76.9% compared with the unmodified coating. Stable lubricating performance was maintained after four consecutive wide-temperature-range thermal cycles, and the COF at 800 °C further decreased to approximately 0.1 with increasing cycle number. It exhibits excellent wear resistance at 800 °C, with a wear rate as low as 0.15×10^{-5} $mm^3/(N \cdot m)$, two orders of magnitude lower than that of the pristine coating (13.86×10^{-5} $mm^3/(N \cdot m)$).

(3) The coating operated via distinct temperature-dependent lubrication mechanisms: micropore storage-graphite interlayer sliding at room temperature, antioxidation barrier-multiphase synergy at medium temperature, and dual-glaze-layer quadruple protection at high temperature. Notably, B_2O_3/Bi_2O_3 played dual critical roles of high-temperature lubrication and graphite oxidation protection, significantly retarding graphite consumption during thermal cycling.

(4) A bilayer glaze layer structure consisting of an amorphous B_2O_3/Bi_2O_3 outer glaze layer and a Cr_2O_3/NiO nanocrystalline inner glaze layer was formed on the wear scar surface at 800 °C. Molecular dynamics simulations revealed the crystalline-to-amorphous liquid transformation pathway of B_2O_3/Bi_2O_3 under high-temperature frictional conditions at the atomic scale, providing theoretical validation for the amorphous phase observed via TEM.

Just Accepted

Supporting information

Supporting information is available from the author.

Declaration of competing interest

The authors declare that they have no known competing financial interests or personal relationships that could have appeared to influence the work reported in this paper.

Data availability

Data will be made available on request.

Acknowledgments

The work was supported by the National Natural Science Foundation of China (No. 52461022), Guangdong Basic and Applied Basic Research Foundation (No. 2025B1515120060), Young Talent Project of GDAS (No. 2024GDASQNRC-0302), GDAS' Project of Science and Technology Development (No. 2024GDASZH-2024010102), GDSTA (No. SKXRC2025045), Young Talent Support Project of Guangzhou Association for Science and Technology (No. QT-2025-019).

References:

[1] Yang X, Li R, Wang Y, et al. Tunable, Wide‐Temperature, and Macroscale Superlubricity Enabled by Nanoscale Van Der Waals Heterojunction‐to‐Homojunction Transformation[J]. Advanced Materials, 2023, 35(39): 2303580.

[2] Ghara T, Kuroda S, Yanagisawa T, et al. Degradation behaviour of HVOF sprayed CoNiCrAlY coating in high-temperature ammonia environment towards its applicability in ammonia fueled gas turbines[J]. International Journal of Hydrogen Energy, 2025, 130: 345-359.

[3] Li T, Hu M, Pei X, et al. Effect of SiC ceramic nano-particles on microstructure and tribological performance of the AlTiVNbNi refractory high entropy alloy in a wide temperature range[J]. Tribology International, 2024, 198: 109850.

[4] Zhang Y H, Sun Y N, Fan X J, et al. Corrosion behavior of WC-NiMoCrFeCo coating in seawater environment: Positive corrosion inhibition of a novel dynamic reaction product[J]. Chemical Engineering Journal, 2025, 507: 160568.

[5] Cheng Q, Jin J, Liu C, et al. Study on the influence mechanism of internal strain on wide-temperature range tribological behavior of Ti6Al4V alloy[J]. Tribology International, 2025, 204: 110488.

Just Accepted

[6] Gao Z, Nie W, Wang H, et al. Enhancing mechanical performance and high-temperature lubrication enabled by MoS2/WB2 nanolayered films[J]. Composites Part B: Engineering, 2024, 275: 111350.

[7] Xu R, Li Z, Meng A, et al. Wear behavior and microstructure evolution of lamellar γ-TiAl alloy at room and elevated temperatures[J]. Tribology International, 2024, 200: 110168.

[8] Wu J, Yang H, Dong P, et al. Effect of various compositions on high-temperature wear failure mechanism of copper-based friction components[J]. Engineering Failure Analysis, 2025, 170: 109275.

[9] Zhang Y, Sun Y, Yang J, et al. Tribological behavior of WC–NiMoCrFeCo coating in seawater environment: Long-term self-lubricating effects of a novel dynamic reaction product[J]. Tribology International, 2025: 111460.

[10] Fotoohinezhadkhales M, Roy A, Ettouil F B, et al. Microstructural insights and temperature effects on wear resistance of CuNiIn coatings: Comparison of HVOF and HVAF processes[J]. Tribology International, 2025, 205: 110541.

[11] Medabalimi S, Hebbale A M, Gudala S, et al. Studies on high temperature erosion behavior of HVOF-sprayed (Cr_3C_2-NiCr) Si and WC-Co/NiCrAlY composite coatings[J]. International Journal of Refractory Metals and Hard Materials, 2025, 127: 106970.

[12] Alroy R J, Kamaraj M, Sivakumar G. Microstructure, property and high-temperature wear performance of Cr3C2-based coatings deposited by conventional and ID-HVAF spray torches: A comparative study[J]. Wear, 2024, 552: 205451.

[13] He D, Mao F, Pan X, et al. Optimizing high-temperature tribological properties of Cr3C2-NiCr/AlCrN duplex coatings by adjusting Cr3C2 contents[J]. Ceramics International, 2025, 51(21): 35181-35192.

[14] Torres H, Rodríguez Ripoll M, Prakash B. Tribological behaviour of self-lubricating materials at high temperatures[J]. International Materials Reviews, 2018, 63(5): 309-340.

[15] Grützmacher P G, Voevodin A A, Korényi-Both A, et al. The promise of solid lubricants for a sustainable future[J]. Advanced Materials, 2026, 38(8): e00867.

[16] Su H, Hu H, Chen S, et al. Tribological properties of atmospheric plasma sprayed Cr3C2–NiCr/20% nickel-coated graphite self-lubricating coatings[J]. Ceramics International, 2024, 50(20): 38040-38050.

Just Accepted

[17] Chen H, Ge M, Qu X, et al. Improved high-temperature tribological properties of Ti3SiC2 modified NiCr-Cr3C2 coatings and their wear mechanism[J]. Surface and Coatings Technology, 2025, 501: 131943.

[18] Su W, Zhang J, Zhang J, et al. Microstructure of HVOF-sprayed Ag–BaF2· CaF2–Cr3C2–NiCr coating and its tribological behavior in a wide temperature range (25° C to 800° C)[J]. Ceramics International, 2021, 47(1): 865-876.

[19] Zheng M, Bian Z, Sun Q, et al. High-temperature tribological performance of (NiCr-20Cr3C2)-2Al-XAg coatings in chloride molten salts[J]. Tribology International, 2025, 205: 110542.

[20] Hu J J, Muratore C, Voevodin A A. Silver diffusion and high-temperature lubrication mechanisms of YSZ – Ag – Mo based nanocomposite coatings[J]. Composites Science and Technology, 2007, 67(3-4): 336-347.

[21] Cheng Y, Zhang Y, Feng Y, et al. Temperature-adaptive MoN-Ag coatings under operando tribology: multiscale Ag diffusion-oxidation coupling[J]. Applied Surface Science, 2025: 164842.

[22] Fang Y, Wu X, Yan J, et al. Effects of Ag Morphology on Tribological Properties and Wear Mechanisms of Ag@ Ti3C2Tx Phosphate Coatings from Room Temperature to 800℃[J]. Tribology International, 2026: 112199.

[23] Zhang Q, Li Y, Liang F, et al. Tailoring tribological characteristics in titanium alloys by laser surface texturing and 2D Ti3C2Tx MXene nanocoating[J]. Advanced Functional Materials, 2024, 34(36): 2401231.

[24] Göçerler H, Danecker C, Gachot C, et al. Unlocking the synergistic impact of laser texturing and Ti3C2Tx MXene coatings – Substrate-specific tribological insights[J]. Carbon, 2025, 238: 120270.

[25] Paknejad M, Bösinger R, Azarhoushang B, et al. Sustainable Tribological Solutions: laser-textured Cr3C2/Cr2O3-Coated Shaft Sleeves[J]. Wear, 2026: 206525.

[26] Wang W, Guo Q, Yuan W, et al. Synergistically Enhanced Tribological Properties and Corrosion Resistance of Ti6Al4V via Laser-Induced Convex Textures[J]. Tribology International, 2025: 111171.

[27] Rosenkranz A, Costa H L, Baykara M Z, et al. Synergetic effects of surface texturing and solid lubricants to tailor friction and wear – a review[J]. Tribology International, 2021, 155: 106792.

Just Accepted

[28] Zhang Y, Li S, Sun Y, et al. Synergistic effects of laser texturing and solid lubricants in Cr3C2-NiCr-(B2O3/Bi2O3) composite coating for enhanced tribological properties at 25° C and 800° C[J]. Tribology International, 2025: 111220.

[29] Li C, Jiao Y, Zhang Y, et al. Noncontact all‐in‐situ reversible reconfiguration of femtosecond laser‐induced shape memory magnetic microcones for multifunctional liquid droplet manipulation and information encryption[J]. Advanced Functional Materials, 2021, 31(20): 2100543.

[30] Kong X, Sun W, Wang Q, et al. Improving high-temperature wear resistance of NiCr matrix self-lubricating composites by controlling oxidation and surface texturing[J]. Journal of Materials Science & Technology, 2022, 131: 253-263.

[31] Wang H, Sun A, Qi X, et al. Wear properties of textured lubricant films filled with graphite and polytetrafluoroethylene (PTFE) via laser surface texturing (LST)[J]. Tribology International, 2022, 167: 107414.

[32] Du G, Zhang Y, Yang G, et al. Wrinkle-engineered self-dispersed MoS 2/graphene hybrids for enhanced high-temperature lubrication[J]. Friction, 2026, 14(7): 9441164.

[33] Huai W, Zhang C, Wen S. Graphite-based solid lubricant for high-temperature lubrication[J]. Friction, 2021, 9(6): 1660-1672.

[34] Wang Z, Zhou X, Zheng K, et al. Simultaneously enhancing heat resistance and mechanical performance for phthalonitrile through in-situ formation of inorganic protective layer derived from low melting point oxide[J]. Composites Part A: Applied Science and Manufacturing, 2023, 174: 107740.

[35] He Z, Wu J. Research on the oxidation process of micro-boron below the melting point temperature[J]. Acta Astronautica, 2024, 225: 67-76.

[36] Jincheng L, Bo W, Jinbao S, et al. Densification mechanisms of Ti2AlC induced by low-melting-point oxide additives during pressureless sintering[J]. Ceramics International, 2025, 51(21): 33273-33281.

[37] Sun H, Jia J, Zhang B, et al. Tribological characteristic of atmospheric plasma sprayed NiAl coatings with addition of nanostructured MoO3/Bi2O3 binary oxides as high temperature lubricant[J]. Journal of Materials Research and Technology, 2022, 17: 1662-1671.

[38] Hou G, Chen J, Geng Y, et al. Thousand-Degree High-Temperature Self-Lubricating “Oil” Achieved by Operando Formation of Liquid B2O3 Through

Just Accepted

Tungsten Tetraboride Superhard Material Tribo-Chemistry[J]. Advanced Functional Materials, 2026: e75711.

[39] Xiao L, Gong W, Long Z, et al. Formation kinetics and equilibrium thermodynamics study on the Bi2O3-TiO2 system for synthesis of the bismuth titanate ceramics[J]. Journal of the European Ceramic Society, 2025, 45(3): 116995.

[40] Sun S, Wang H, Liu X, et al. Outstanding anti-oxidation performance of boride coating under high-temperature friction[J]. Corrosion Science, 2021, 179: 109133.

[41] Shao X, Ren Y, Guo K, et al. Achieving high temperature lubrication of MoS2-Bi2O3 nanoparticles composite: Through the formation of nanocrystalline ternary oxide and glaze layer[J]. Tribology International, 2025, 206: 110577.

[42] Chen Y, He Z, Jiao J, et al. Glass-forming region and properties of CuO-Bi2O3-B2O3 low-melting glass for laser/infrared radiation sealing[J]. Journal of Alloys and Compounds, 2025: 183047.

[43] Zhang K, Lin Z, Chen J, et al. An ingenious synergistic solid lubricant of copper and graphite for exceptional wear resistance of the SCF/PTFE/PEEK composite[J]. Tribology International, 2024, 195: 109583.

[44] Somberg J, Gonçalves G, Emami N. Graphene oxide versus graphite and chemically expanded graphite as solid lubricant in ultrahigh molecular weight polyethylene composites[J]. Tribology International, 2023, 187: 108643.

[45] Chen Z, Fan H, Tan H, et al. Effects of graphite contents on the microstructure evolution, mechanical properties and high temperature tribological behavior of Cu－Ni－Al/Gr solid-lubricating composites[J]. Tribology International, 2023, 179: 108193.

[46] Cheng P, Wang R, Hu Z, et al. Enhancing high-temperature tribological properties of graphite-modified CFRP composites through interfacial engineering with in situ formed metal oxides[J]. Carbon, 2026: 121564.

[47] Zhai L, Liu Y, Yang K, et al. Enhanced self-lubrication and anti-wear of bio-inspired surface through synergy of laser-induced hexagonal textures and solid lubrication[J]. Tribology International, 2026: 112252.

[48] Bharath H, Venkatesan K. Investigation of machinability characteristics of Inconel 713C using new novel honeycomb and broken-parallel texture cutting inserts with graphene-based solid lubricants[J]. Journal of Manufacturing Processes, 2024, 109: 643-668.

Just Accepted

[49] Biswas A, Sapkota P K, Kazibwe S, et al. A Semiconductor Composite with High Solid‐State Lubrication and Low Thermal Conducting Properties[J]. Advanced Functional Materials, 2026, 36(26): e25251.

[50] Greiner C, Gagel J, Gumbsch P. Solids under extreme shear: Friction‐mediated subsurface structural transformations[J]. Advanced Materials, 2019, 31(26): 1806705.

[51] Pei X, Zhang J, Wang H, et al. In Situ Crystalline-Amorphous Composite Oxide Structure Suppressing Thermal Wear Instability for Refractory Multi-Principal Element Alloy[J]. Advanced Functional Materials, 2026: e76064.

[52] Gao Y, Ma JJ, Chen Y, Wang M. Effect of Bi_2O_3 on the structure and thermal properties of Bi_2O_3-SiO_2-B_2O_3 glasses prepared by sol-gel method. Journal of Sol-Gel Science and Technology, 2022, 103(3):713-721.

[53] Li B, Gao Y, Li C, Kang Y, Hou X, Liu F, Zhao S. Improved tribological performance of nickel based high temperature lubricating composites with addition of metallic oxides. Wear, 2021, 480:203938.

[54] Dudziak T, Deodeshmukh V, Backert L, et al. Phase Investigations Under Steam Oxidation Process at 800 °C for 1000 h of Advanced Steels and Ni-Based Alloys[J]. Oxidation of Metals, 2017, 87(1–2): 139–158.

Just Accepted